GA–A24948

EXPERIMENTAL SIGNATURES OF HOMOCLINIC TANGLES IN POLOIDALLY DIVERTED TOKAMAKS

by
T.E. EVANS, R.K.W. ROEDER, J.A. CARTER, B.I. RAPOPORT,
M.E. FENSTERMACHER, and C.J. LASNIER

JANUARY 2005

GENERAL ATOMICS

DISCLAIMER

GA–A24948

EXPERIMENTAL SIGNATURES OF HOMOCLINIC TANGLES IN POLOIDALLY DIVERTED TOKAMAKS

by
T.E. EVANS, R.K.W. ROEDER,* J.A. CARTER,† B.I. RAPOPORT,‡
M.E. FENSTERMACHER,§ and C.J. LASNIER§

This is a preprint of a paper to be presented at the International Workshop on Chaotic Transport and Complexity in Fluids and Plasmas, Carry Le Rouet, France, June 20–25, 2004 and to be printed in the Journal of Physics: Conference Series.

*Cornell University, Ithaca, New York
†Massachusetts Institute of Technology, Cambridge, Massachusetts
‡Harvard University, Cambridge, Massachusetts
§Lawrence Livermore National Laboratory, Livermore, California

Work supported by
the U.S. Department of Energy under
DE-FC02-04ER54698 and W-7405-ENG-48

GENERAL ATOMICS PROJECT 30200
JANUARY 2005

GENERAL ATOMICS

ABSTRACT

Small non-axisymmetric perturbations of poloidally diverted tokamaks create edge stochastic magnetic field lines that connect to material surfaces such as those in the divertors. Separatrix structure calculations show that the distribution of stochastic field lines on the vessel walls is closely related to the topology of homoclinic tangles formed in the perturbed system. Since these tangles prescribe how the stochastic fields are organized, they are of significant practical interest in tokamak experiments. Experimental measurements of heat and particle distributions on plasma facing surfaces sometimes show split peak patterns that are consistent with the presence of stochasticity and homoclinic tangles. These split peaks are often observed during locked modes and other types of edge instabilities. They are also observed when perturbation fields from magnetohydrodynamic control coils are pulsed during a plasma discharge. Numerical modeling of the perturbation field from these control coils shows that the homoclinic tangle produced by a coil pulse is not always large enough to produce the splitting patterns observed. Nevertheless, there is a clear correlation between the coil pulses and the appearance of the split profiles. These results suggest the presence of the plasma amplification mechanism that enhances the size of the non-resonant homoclinic tangles.

1. INTRODUCTION

The magnetic separatrix of a poloidally diverted tokamak is commonly envisioned as a 2D axisymmetric boundary that divides magnetic field line trajectories of the closed inner, confined plasma, domain from the outer scrape-off layer plasma region where field lines intersect divertor target plates within relatively short distances. In reality, the magnetic separatrix in poloidally diverted tokamaks is a relatively fragile structure that is easily split into a pair of intersecting invariant manifolds by small non-axisymmetric magnetic perturbations. Such perturbations are known to be present in all practical toroidal confinement systems such as tokamaks and stellarators due to unintentional misalignments of external coils (i.e., field-errors), ensemble or intrinsic topological noise effects (i.e., from random tolerance build ups, unbalanced thermal, mechanical and electromagnetic forces and the relaxation of materials in all the coils that make up the confinement system with age), non-axisymmetric control coils [e.g., correction, resistive wall mode or other magnetohydrodynamic (MHD) coils] and from internal MHD modes or non-axisymmetric current filaments driven by plasma potentials. This type of splitting is a generic property of perturbed nonlinear dynamical systems with hyperbolic fixed points [1,2] (referred to as x-points in the tokamak literature). Since perturbed vacuum magnetic field lines in toroidal plasma confinement devices represent a differential system that is described at an elementary level by the theory of near-integrable conservative Hamiltonian dynamics, we expect to find that the existence of complex topologies characterizing the state of the system is not uncommon. In Section 2 we outline the basic theory of Hamiltonian field line theory in tokamaks and in Section 3 we present calculations of homoclinic tangles found in the perturbed equilibrium field of the DIII–D tokamak using a sophisticated field line mapping code. Section 4 summarizes the experimental measurements made in DIII–D and other tokamaks that are representative of signatures expected to be produced by homoclinic tangles and in Section 5 we summarize the results and conclusions.

2. BASIC HAMILTONIAN DESCRIPTION OF MAGNETIC FIELD LINES IN POLOIDALLY DIVERTED TOKAMAKS

The simplest analytic construction of a poloidally diverted tokamak equilibrium is obtained using a two or three wire model with axisymmetric circular symmetry about the major axis. Here, one wire simulates the plasma current while the others represents the current in the divertor coils. Examples of such a models are discussed by Pomphery and Reiman [3] and by Abdullaev and Finken [4]. Recently, a more realistic model, developed by Evans, Moyer and Monat [5], has been used to study stochastic magnetic field line flux loss from the pedestal region of poloidally diverted plasmas as a function of the equilibrium shape and edge safety factor profile. In this model the unperturbed axisymmetric magnetic equilibrium is first calculated using a Grad-Shafranov solver known as the EFIT code [6] where surfaces of constant poloidal magnetic flux ψ are calculated by adjusting the toroidal plasma current density profile while conserving the total plasma current and the safety factor [$q(\Phi) = d\Phi/d\psi$ defined below by equation (5) where Φ is the toroidal magnetic flux] on axis. The equilibrium calculation is constrained by measurements of the poloidal magnetic field outside the plasma and is required to satisfy an MHD force balance condition that is consistent with the calculated toroidal current density, plasma pressure and poloidal current profile. An example of such an equilibrium reconstruction in the DIII–D [7] tokamak is given in Fig. 1 which shows closed contours of constant ψ (forming toroidal surfaces) inside the unperturbed equilibrium separatrix and an open ψ contour outside the separatrix. With this representation, ψ defines a monotonic radial-like variable and the poloidal angle θ defines an angular location on ψ at any toroidal angle ϕ.

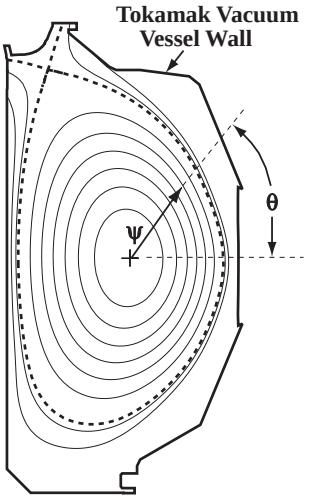

Fig. 1. Poloidal cross-section of the DIII–D tokamak showing the solid vessel wall and contours of ψ (flux surfaces).

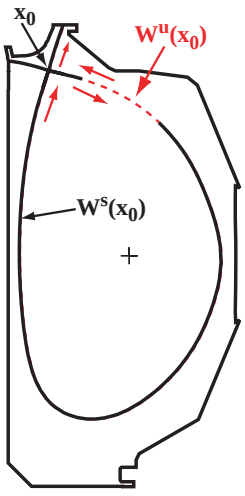

Fig. 2. The unperturbed separatrix due to $\times_0$ is made up of an unstable manifold $W^U(\times_0)$ covered by a stable $W^S(\times_0)$.

The equilibrium separatrix is composed of a stable $W^S(\times_0)$ and an unstable $W^U(\times_0)$ manifold associated with the hyperbolic fixed point $\times_0$ shown in Fig. 2. It should be recalled that (un)stable invariant manifolds of a nonlinear system are divided into two sets representing the generalized eigenspaces associated with a hyperbolic fixed point or x-point. The eigenvalues associated with a hyperbolic fixed point $\times_0$ are λ_s, the stable eigenvalue, satisfying $|\lambda_s|<1$ and λ_u, the unstable eigenvalue, satisfying $|\lambda_u|>1$. The eigenvalues define the eigenvectors of the stable manifold $W^S(\times_0)$ and the unstable manifold $W^U(\times_0)$ respectively. Thus, as shown in Fig. 2, solution trajectories approach $\times_0$ along the stable manifold $W^S(\times_0)$ and move away from $\times_0$ along the unstable manifold $W^U(\times_0)$. Here, a section of $W^S(\times_0)$ has been removed to show $W^U(\times_0)$ since these manifolds overlay each other in the absence of non-axisymmetric magnetic perturbations. As discussed in [8], magnetic field line trajectories passing through the poloidal plane shown in Figs. 1 and 2 asymptotically approach $\times_0$ along the (un)stable manifold as ϕ (decreases)increases. Using $\vec{B}=\nabla\times\vec{A}=B_r\hat{e}_r+B_\theta\hat{e}_\theta+B_\phi\hat{e}_\phi$ we may express the magnetic field in terms of toroidal Φ and poloidal ψ magnetic flux functions using:

$$\vec{B}=\nabla\Phi\times\nabla\theta-\nabla\psi\times\nabla\phi \quad . \tag{1}$$

Combining $(d\Phi,d\theta,d\phi)=\vec{B}\bullet(\nabla\Phi,\nabla\theta,\nabla\phi)$ with equation (1) we have:

$$\frac{d\Phi}{d\phi}=\frac{\vec{B}\bullet\nabla\Phi}{\vec{B}\bullet\nabla\phi}=-\frac{(\nabla\psi\times\nabla\phi)\bullet\nabla\Phi}{(\nabla\Phi\times\nabla\theta)\bullet\nabla\phi}=-\frac{\partial\psi/\partial\theta(\nabla\theta\times\nabla\phi)\bullet\nabla\Phi}{(\nabla\Phi\times\nabla\theta)\bullet\nabla\phi} \tag{2}$$

and

$$\frac{d\theta}{d\phi}=\frac{\vec{B}\bullet\nabla\theta}{\vec{B}\bullet\nabla\phi}=-\frac{(\nabla\psi\times\nabla\phi)\bullet\nabla\theta}{(\nabla\Phi\times\nabla\theta)\bullet\nabla\phi}=-\frac{\partial\psi/\partial\Phi(\nabla\Phi\times\nabla\phi)\bullet\nabla\theta}{(\nabla\Phi\times\nabla\theta)\bullet\nabla\phi} \tag{3}$$

where we see that equations (2) and (3) reduced respectively to:

$$\frac{d\Phi}{d\phi}=-\frac{d\psi}{d\theta} \tag{4}$$

and

$$\frac{d\theta}{d\phi}=\frac{d\psi}{d\Phi} \tag{5}$$

Associating $\psi(\Phi,\theta,\phi)$ with a Hamiltonian $H(\Phi,\theta,\phi)$ we see that equations (4) and (5) describe magnetic field line trajectories on toroidal flux surfaces. Thus, we identify field line trajectories in toroidal plasmas with a conservative Hamiltonian dynamical system where the toroidal angle ϕ serves as a time-like variable of the dynamics. For unperturbed axisymmetric cases $H(\Phi,\theta)=H_0$. Assuming typical tokamak plasma current profiles, the field lines form helical trajectories with a monotonically decreasing pitch angle compared to the equatorial plane as Φ increases from the magnetic axis to the separatrix. This changing magnetic field pitch angle, when averaged over a flux surface, is referred to as the safety factor $q(\Phi)$ and is defined as the rate of change in toroidal magnetic flux Φ with respect to the poloidal magnetic flux ψ, $q(\Phi)=d\Phi/d\psi$. Thus, as seen from equation (5) the change in the poloidal angle $d\theta$ of a field line decreases with increasing $q(\Phi)$ for constant steps in the toroidal

angle $d\phi$. This is a consequence of radial shear in the magnetic field and results in a differential twist of the field lines from one flux surface to the next.

A magnetic field line integration code, referred to as the TRIP3D code [5], is used to calculate 3-space field line trajectories in poloidally diverted tokamaks such as DIII–D. The code numerically integrates field line trajectories prescribed by equations (4) and (5) where the components associated with the axisymmetric part of the Hamiltonian H_0 are calculated directly from an EFIT equilibrium solution using the second term in equation (1) for the poloidal magnetic field B_θ and the EFIT $F(\psi)$ function [$F(\psi) = R B_T$] where R is the major radius of the plasma equilibrium and B_T is the toroidal magnetic field]. Here, $F(\psi)$ accounts for both the poloidal currents from external coils and poloidal part of the plasma current. This part of the magnetic field represents the combined axisymmetric vacuum/plasma Grad-Shafranov equilibrium which is required to accurately model shaped, poloidally diverted, plasmas with self-consistent radial plasma pressure and current density profiles. Non-axisymmetric perturbation fields enter the Hamiltonian in the following form:

$$H(\Phi,\theta,\phi) = H_0 + \sum_{i,j=1,1}^{n,m} \varepsilon_{i,j} H_{i,j}(\Phi,\theta,\phi) \tag{6}$$

where $\varepsilon_{i,j}$ is the amplitude of the i,j Fourier modes (with m being the poloidal mode number and n the toroidal mode number) summed over all perturbation sources since there are numerous sources of perturbations in tokamak environments. The TRIP3D code calculates vacuum magnetic field line trajectories due to all the perturbation sources at any $\psi(\Phi,\theta,\phi)$ in the plasma domain (including open field lines that intersect solid material surfaces) using a realistic geometric representation of the source and an algorithm based on the Biot-Savart magnetic induction law. For the studies discussed here the TRIP3D code is used to construct a numerical twist map of the field line intersections with a Poincaré surface. This code is referred to as TRIP3D_MAP. Using TRIP3D_MAP field line trajectories that pass through a Poincaré surface, such as the poloidal surfaces shown in Figs. 1 and 2, field lines are mapped back to the surface by advancing ϕ through an integer number N of 2π steps. Thus, N is the iteration index of a Poincaré plot that shows position of a field line trajectory or group of trajectories as they pass through a Poincaré surface of interest.

3. CALCULATIONS OF INVARIANT MANIFOLDS AND HOMOCLINIC TANGLES IN TOKAMAKS

Invariant manifolds associated with a hyperbolic fixed point of the TRIP3D_MAP, such as $\times_0$ in Fig. 2, are calculated by constructing the (un)stable eigenvectors $\vec{e}_{(u),s}$ associated with a fixed point $\times$ and populating a line segment directed along $\vec{e}_{(u),s}$ with a set of evenly distributed points. Then $W^U(\times)$ is approximated by mapping the points distributed along the $\vec{e}_u$ direction on to a Poincaré surface using N successive forward iterations of the TRIP3D_MAP while the stable manifold associated with $\times$ is calculated by applying N inverse iterations of the map to the points distributed along the $\vec{e}_u$ direction. The (un)stable manifolds are represented on the Poincaré surface by connecting the resulting points with solid curves. An example of such a calculation is shown in Fig. 3(a) where the poloidal Poincaré surface has been cut at $\theta = 0$ and unfolded. In addition, the radial extent in Φ_N covers only the outer part of the plasma in order to better resolve small spatial structures associated with the invariant manifolds (solid curves) and to better visualize magnetic field line trajectories as they pass through the Poincaré surface (small solid dots). This calculation was done with a circular flux surface version of TRIP3D_MAP referred to as TRIP_MAP [5] and the non-axisymmetric perturbations used here are due to small (~2–9 mm) random shifts of all the external tokamak coils. These types of perturbations are referred to as ensemble or intrinsic topological noise effects [9] that are associated with random shifts due to engineering design tolerances in the coil assemblies as well as non-ideal effects such as unbalanced thermal and electromagnetic forces that occur during the operation of the machine. Such perturbations are always present to some degree in complex magnetic machines such

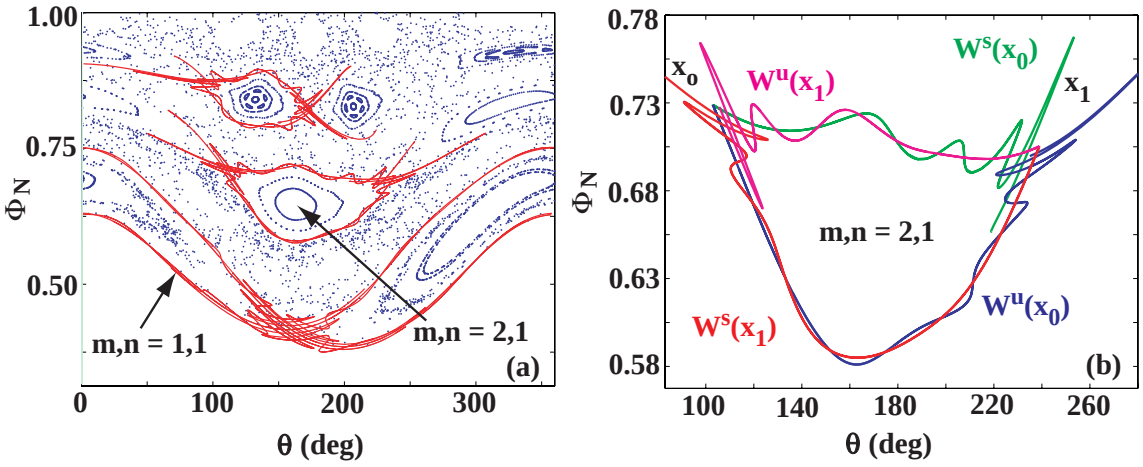

Fig. 3. (a) Poincaré section showing (un)stable invariant manifolds (solid lines) associated with three sets of resonant magnetic island chains. The solid dots are field line trajectories that have been mapped to the Poincaré section using TRIP_MAP, (b) an expanded view of the invariant manifolds associated with hyperbolic points of the $m,n = 2,1$ island chain.

as a tokamak and are particularly difficult to measure or to systematically quantify. Simulations of such effects demonstrate that they can be as significant as field-errors due to multi-millimeter misplacements of individual coils [9]. The detailed structure of the (un)stable manifolds associated with the two hyperbolic fixed points, $\times_0$ and $\times_1$, of the $m,n=2,1$ island chain (m and n are the poloidal and toroidal mode numbers of the island chains), shown in Fig. 3(a), are given in Fig. 3(b). Here, the (un)stable manifolds $W^{(u)s}(\times_0)$ associated with $\times_0$ oscillate wildly as they approach $\times_1$. Both $W^s(\times_1)$ and $W^u(\times_1)$ display similar behaviors as they approach $\times_0$. Such oscillations are a generic feature of resonant invariant manifolds surrounding magnetic islands in tokamaks and have been calculated using TRIP3D_MAP in DIII–D for equilibria perturbed by a set of correction coils [10] used to inhibit the locking of core MHD modes to measured field-error. Intersections of the stable and unstable manifolds from individual hyperbolic fixed points define lobes within a structure referred to as homoclinic tangles [1] and these lobes can overlap near the hyperbolic points as shown in Fig. 3(b). This overlapping of lobes defined by a stable manifold with lobes defined by an unstable manifold causes stochastic mixing of the field lines near the hyperbolic fixed points of the resonant islands. It is important to note that stable manifolds may not intersect other stable manifolds and unstable manifolds may not intersect other unstable manifolds since this would result in solutions of equations (4) and (5) that are not unique.

As the amplitude of the perturbation is increased in TRIP_MAP, for the case shown in Fig. 3, the resonant homoclinic tangles associated with the $m,n=2,1$ and $m,n=3,1$ islands intersect and field lines are exchanged between neighboring island chains. The trajectories of the field lines involved in this inter-island exchange are quite complex as can be seen in Fig. 4. This process of magnetic flux

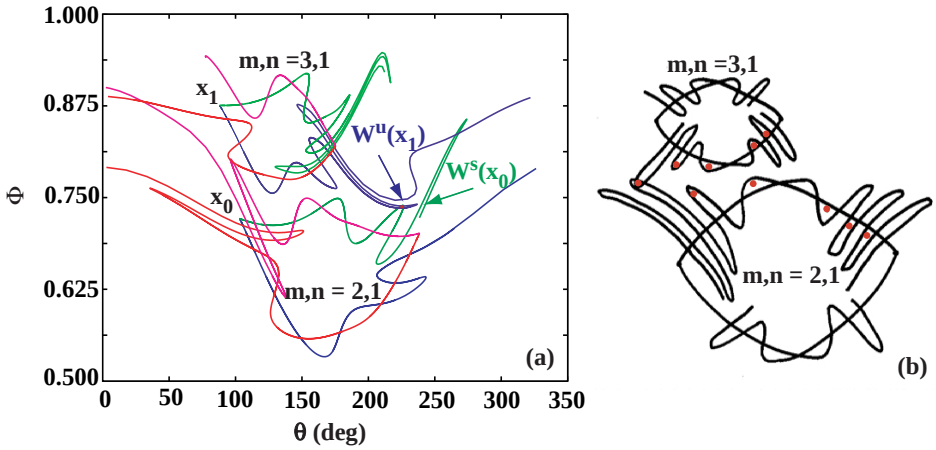

Fig. 4. (a) A stable manifold associated with the $\times_0$ hyperbolic point of the $m,n=2,1$ island shown in Fig. 3(a) intersects the unstable manifold of the $m,n=3,1$ island with an increase in the perturbation amplitude in TRIP_MAP and (b) conceptualization of field line mixing between neighboring islands such as those shown in (a). The solid dots represent the position of a field line that is exchanged between islands through the intersection of a stable lobe in one island and an unstable lobe of the neighboring island as the map is iterated.

exchange through the lobes of homoclinic tangles is the mechanism that leads to the onset of global magnetic stochasticity and the radial transport of field lines in tokamaks. In circular tokamaks, i.e., those without an unperturbed equilibrium separatrix, stochastic field lines are transported to solid surfaces such as the vacuum vessel walls through intersections of interior island resonant homoclinic tangles with tangles surrounding islands near the plasma boundary. Stochastic magnetic flux transport due to resonant tangle intersections between magnetic islands in the edge plasma of a circular tokamak has recently been studied by a group in Brazil [11] and has been found to produce complex magnetic footprints on the vacuum vessel walls.

In poloidally diverted tokamaks, magnetic flux transport to solid surfaces such as divertor target plates involves the interaction of both resonant tangles surrounding interior islands and non-resonant homoclinic tangles that form on the equilibrium separatrix when non-axisymmetric magnetic perturbations are present in the system. While resonant island and non-resonant separatrix tangles both involve a splitting of the separatrices into stable and unstable manifolds, magnetic island separatrix splitting is produced by helical perturbations (with m,n poloidal and toroidal mode numbers) that are resonant on mode rational surfaces $q(\Phi) = d\Phi/d\psi = m/n$ while non-resonant equilibrium separatrix tangles result from a linear superposition of amplitudes and phases defined by all the non-axisymmetric perturbations of the system. This is a consequence of the fact that hyperbolic fixed points associated with the resonant island tangles are helical in nature while fixed points associated with an equilibrium separatrix are strictly axisymmetric and thus form non-resonant tangles. Numerical modeling, comparing the stochastic flux loss in circular and diverted cases, has demonstrated that the width of the flux loss layer is significantly broader at low perturbation amplitudes in diverted plasmas [5]. Calculation of the splitting threshold in DIII–D have shown that perturbation fields of 0.8 G (approximately the magnitude of the Earth's magnetic field and a factor of ~30 below the magnitude of the measured field-errors in DIII–D) produce tangles with centimeter scale lobes surrounding equilibrium hyperbolic fixed points in DIII–D [10]. The details of the equilibrium separatrix splitting are rather sensitive to the number of axisymmetric hyperbolic points (e.g., one for single null poloidally diverted plasmas and two for double null plasmas although additional hyperbolic points can be introduced in machine designs with more divertor coils), the radial and vertical positions of the hyperbolic points (referred to as the triangularity and vertical gap dimensions), the up-down symmetry of the hyperbolic points in double null plasmas and a variety of other flux surface shape parameters.

The effects of variations in the flux surface shape parameters on the topology of the perturbed equilibrium separatrix tangles has been studied using TRIP3D_MAP in DIII–D. It was found that double null plasmas demonstrate particularly complex sequences of tangle bifurcations as the up-down symmetry of the hyperbolic fixed points is varied over a relatively small range using a parameter referred to as dR_{sep} [8]. Plasmas with upper and lower hyperbolic fixed points equally spaced above and below a horizontal plane defined by the magnetic axis of the plasma have $dR_{sep} = 0$, meaning that the unperturbed outer separatricies associated with these fixed points overlay each other when intersecting the horizontal magnetic axis plane. In this situation the (un)stable manifolds associated

with the lower hyperbolic point oscillate wildly as they approach the upper hyperbolic point and the manifolds associated with the upper hyperbolic point oscillate as they approach the lower hyperbolic point. This results in an up-down symmetric pair of tangles with lobes that have finger-like structures extending out across both the inner and outer open flux surface region (i.e., referred to as the scrape-off layer) of the upper and lower divertors. Relatively small changes in the dR_{sep} parameter result in a dramatic bifurcation of the tangles and the finger-like structures they produce in the divertors. An example of the tangle topology calculated in TRIP3D_MAP with dR_{sep} = –0.008 m and an $n=1$ perturbation field is due only to a 10 kA-turn current in the error-field correction coil (the DIII–D C–coil [5]) is shown in Fig. 5. Here we see a relatively large oscillation in the $W^U(\times_0)$ manifold in the outer scrape-off layer region of the upper divertor. Several broad lobes of the tangle formed by $W^U(\times_0)$ and $W^S(\times_0)$ penetrate the horizontal plane at Z = 1.10 m and a series of thinner lobes "pile up" and stretch out toward the upper divertor target plate located at an elevation of 1.35 m. There are an infinite number of these thin lobes that intersect the divertor target plate. These lobes create a hyperfine structure of intersections across a small region of the target plate near the location of the unperturbed the strike point. A similar but somewhat more complex structure exists in the lower divertor for this case. Here we see that the $W^S(\times_0)$ and $W^S(\times_1)$ manifolds shadow each other (since they are not allowed to intersect) as they approach the lower hyperbolic fixed point. The manifolds form a double bounded tangle with $W^U(\times_0)$ that adds a higher order component to the hyperfine structure of intersections across the outer strike point region of the lower divertor target plate. Since the manifolds defining the lobes shown in Fig. 5 intersect manifolds that are associated with resonant island hyperbolic points deeper inside the plasma, escape pathways are formed that result in the stochastic transport of field lines radially outward into the protruding finger-like structures. Thus, if viewed normal to the Poincaré plane the tangles will look like filaments filled with hot plasma streaming out along the stochastic field lines from relatively deep inside the plasma. To estimate the radial extent over which the field line trajectories inside these scrape-off layer filaments move, a set of initial field line starting points were selected in the tip of a $W^U(\times_0)$ lobe that penetrates the upper divertor target plate shown in Fig. 5. With these initial conditions and the same parameters as those used for the calculations shown in Fig. 5, TRIP3D_MAP was iterated backwards over three $N=8$ iterations and the positions of the field lines were plotted on the Poincaré section for each set of eight iterations. Many of the field lines randomly crossed the outer pedestal region and several reached the top of the pedestal. Base on these results it is not unreasonable to expect that field lines from the region near or inside $q=2$, with relatively short lengths, may connect ("short out") the divertor targets to the hot core plasma when magnetic perturbations from all the sources found in DIII–D (e.g., field-errors, intrinsic topological noise, and MHD fields) are included in this calculation.

A key feature of these separatrix tangles is their footprint on solid surfaces such as the upper and lower divertor target plates. The toroidal structure of these footprints on the upper divertor target has been studied for the tangles shown in Fig. 5 [10]. Similar footprints have been found using simplified two or three wire models [3,4]. An example of such a footprint calculated with TRIP3D_MAP is shown in Fig. 6. Here a horizontal plane located at Z = 1.10 m as shown in Fig. 5 is used to image the toroidal outline of the tangle as it penetrates the plane. This particular plane is selected to provide a

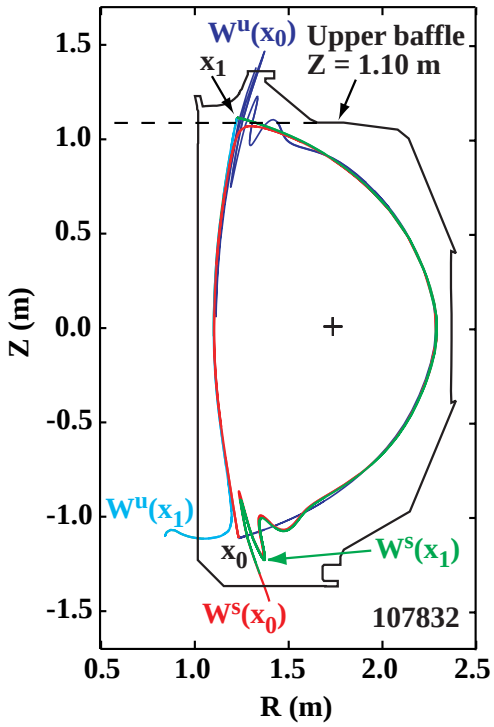

Fig. 5. Poloidal cross-section of the DIII–D tokamak showing the solid vessel wall and homoclinic tangles formed by the splitting of invariant manifolds associated with each of the axisymmetric hyperbolic fixed points in a relatively well balanced double null diverted plasma.

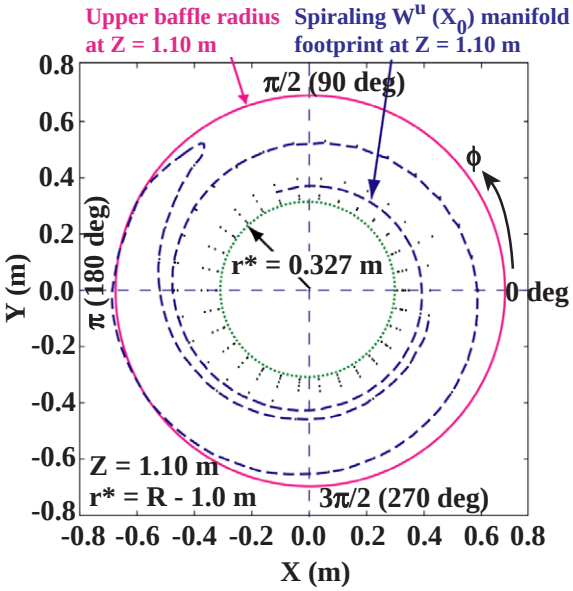

Fig. 6. Toroidal pattern made by $W^U(\times_0)$ in Fig. 5 when projected on the $Z = 1.1$ m plane. The upper baffle radius on the projection plane is indicated and the unperturbed outer separatrix strike point at the $Z = 1.35$ m upper divertor solid surface is indicated as $r* = 0.327$ m.

quantitative estimate of the extent of the spatial coverage by the tangle lobes at a point where a tangential camera may see such structures in the scrape-off layer and to highlight the fact that tangles can produce toroidally asymmetric “hot spots” on objects that protrude into the scrape-off layer. We see a well defined spiral on the image plane with several distinct radial lobes at some toroidal angles. We also note that the outer edge of the spiral tip touches the upper baffle near $\phi = \pi$ rad (180 deg). Infrared cameras in DIII–D sometimes observe hot spots on this baffle particularly when the plasma current is run in a direction opposite to that of the neutral beam injection during Quiescent H–modes or when large MHD modes are excited in the plasma. The full 3D topology of a tangle similar to the one shown in figures 5 and 6 is given in Fig. 7. Here, the spiraling filament-like tangle has an $n = 1$ structure which defined by the magnetic perturbation from the DIII–D error-field correction coil. It should be noted that higher n perturbations produce higher n spiral-like footprints on the divertor targets [4] and that a change in the toroidal phase of the perturbation rotates these spirals around in toroidal angle with the phase of the perturbation. If more than one perturbation source is present the shape of the spiral has a toroidal variation that depends on the linear superposition of the amplitudes and phases of all the perturbation. Thus, a rotating mode such as a neoclassical tearing mode or a

quasi-stationary locked mode produces a time varying modulation of the toroidal structure of this footprint. These facts will be useful to keep in mind below as we discuss the experimental observations of these footprints in the divertors.

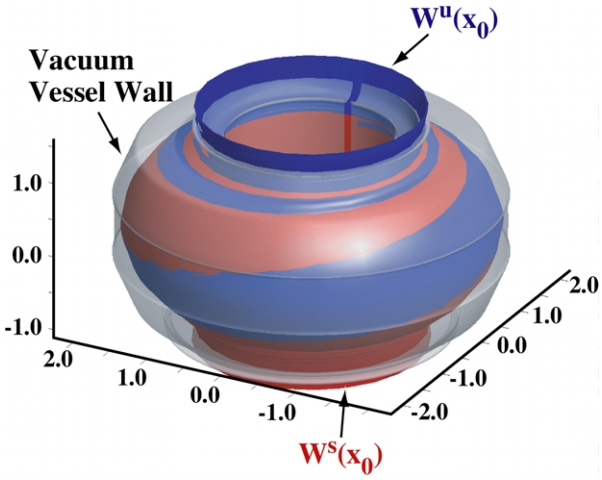

Fig. 7. A view of the topology of a homoclinic tangle such as the one shown in Figs. 5 and 6. The lobes of the tangle formed by the stable and unstable manifolds are imaged on the toroidal surface defined by the unperturbed equilibrium separatrix. The spiral bands connect to form a continuous a helical filament-like structure with a corkscrew like topology wrapped around the torus. The helical "corkscrew-like" bands are the images of the stable (light) and unstable (dark) manifolds on the separatrix surface.

4. EXPERIMENTAL OBSERVATIONS

Measurements of toroidal heat flux asymmetries in the DIII–D divertors have demonstrated that features such multipeaked radial profiles are not uncommon in many plasma discharges. Such features are particularly large during so-called locked modes in DIII–D but they are also present in a variety of other discharges. The first toroidally and radially resolved measurements of these heat flux asymmetries showed that they are sometimes made up of two peaks separated radially by ~5 cm as seen by an infrared camera at ϕ = 60 deg and simultaneously by the same two peaks but with an additional peak of approximately the same amplitude located ~15 cm radially outward from the first peak as seen by an infrared camera at ϕ = 165 deg [12]. Comparing these heat flux profiles to the toroidal image of the homoclinic tangle shown in Fig. 6 above we can easily associate the double peak heat flux structure at ϕ = 60 deg with the radial profile of the tangle along the x axis between y = 0.33 m and y = 0.5 m (at $\phi = \pi/2$) while the triply peaked structure observed at ϕ = 165 deg qualitatively agrees with the spiral tangle distribution in the third quadrant at a 15 deg angle below the y axis (ϕ = 195 deg) from the unperturbed equilibrium separatrix out to the radius of the baffle. Similar flux measurements during MHD events in VH–modes have shown that these split peak distributions are sensitive to perturbations from internal MHD modes and that they change rapidly as the mode amplitude and phase evolves [12]. High time resolution measurements of heat flux distributions on the divertor target plates in the ASDEX–U tokamak have recently shown that the impulsive energy losses due to edge localized modes (ELMs) also produce profiles with multiple peaks in the radial direction during the ELM crash [13]. In addition, the ASDEX–U data shows that these striped peaks produced by ELMs have an inclination angle with respect to the toroidal magnetic field that suggests they are part of a larger spiral structure. The first measurements of toroidal asymmetries due to ELMs were made using a toroidal tile current array in DIII–D [12]. The measurements showed that large non-axisymmetric currents are driven in the scrape-off layer during an ELM crash which can presumably influence the topology of resonant islands and equilibrium separatrix tangles. Similar but significantly larger non-axisymmetric scrape-off layer currents (sometimes referred to as halo currents) are also measure during disruptions in DIII–D with the toroidal tile current array [12] and recent measurements with this diagnostic have shown that these non-axisymmetric currents are often present during and correlated with core MHD activity in many discharges or with edge harmonic oscillations that are often observed during DIII–D QH–modes [14].

Experiments using an internal magnetic perturbation coil (referred to as the I–coil) have been quite successful in suppressing large ELMs in DIII–D [15]. Figure 8 shows how the I–coil pulse, starting a t = 3000 ms, affects the peak in the lower divertor heat flux near the outer strike point compared to a discharge without the I–coil pulse. The upper trace in Fig. 8(b) shows the time evolution of the peak in the amplitude of the radial heat flux profile (as indicated by the peak in the lower divertor curve near the outer strike point in Fig. 9) and the lower curve in Fig. 8(b) shows the change in this peak during the magnetic perturbation pulse from the I–coil starting at t = 3000 ms as indicated in

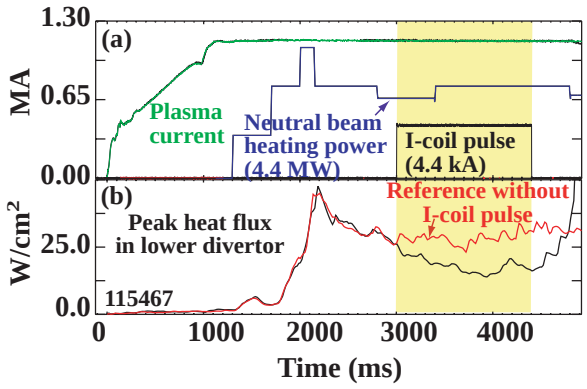

Fig. 8. (a) Plasma current, injected neutral beam power and I–coil magnetic perturbation current pulse in DIII–D ELM suppression discharge 115467 and (b) peak heat flux in the lower divertor (as shown in Fig. 10) with (lower) and without (upper) the magnetic perturbation field.

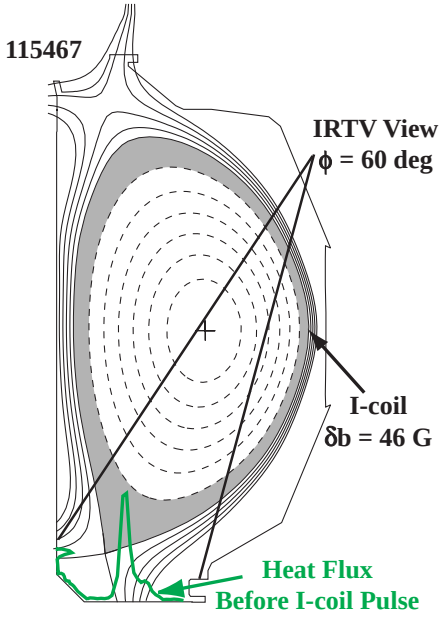

Fig. 9. DIII–D equilibrium shape used during the ELM suppression experiment in discharge 115467 (as shown in Fig. 8). The view used by the infrared TV camera at ϕ = 60 deg is shown along with a conceptual illustration of the amplitude of the heat flux distribution on the divertor.

Fig. 8(a). Figure 9 shows the view of the infrared (IR) TV camera and indicates that the total field due to the I–coil current pulse is 46 G at the midplane near the outer unperturbed equilibrium separatrix. Using data from this discharge we plot the radial distribution of the heat flux as a function of time in Fig. 10(a). Here, we see that the peak located near the outer divertor strike point at R = 134 cm splits into a pair of peaks with roughly half the amplitude and separated by ~5 cm. We also note that when the magnetic perturbation pulse from the I–coil ends at t = 4400 ms the original peak recovers and the secondary peak diminishes in amplitude. Figure 10(b) shows the radial profile of the heat flux plotted in Fig. 10(a) at t = 2900 ms, before the perturbation pulse from the I–coil, and during the perturbation pulse at t = 3300 ms. Looking at Fig. 10(a) again, we see that there is a continuous change in the amplitude of the two heat flux peaks yet the perturbation field from the I–coil is constant. We interpret this to be evidence of a non-stationary component in the total perturbation field that modulates the structure of the tangle footprint on the divertor target plate. Interestingly, we know that the plasma rotation is strongly damped during this time and that rapidly rotating core MHD modes are slowing down to the point that perturbations from their magnetic fields could be visible on the relatively slow time scale of this particular measurement. These MHD mode are observed to slow down with the plasma and stop rotating for a shot time then spin up again slowly later in the I-coil pulse. Since we do not expect perturbations from field-errors or intrinsic topological noise to change on this time scale and no other sources of external magnetic perturbations were being used during this discharge (i.e.,

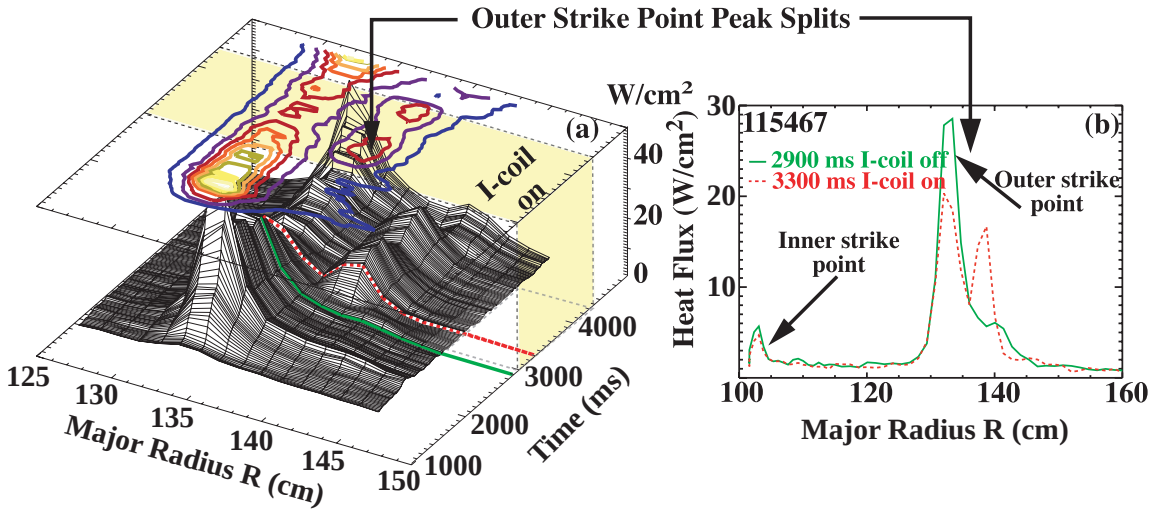

Fig. 10. (a) Evolution of the radial heat flux profile in the lower divertor during an ELM suppression discharge where the magnetic perturbation from the DIII–D I–coil is pulsed starting at t = 3000 ms. This data was obtained during the discharge shown in Fig. 8 using the infrared camera view shown in Fig. 9 and (b) two radial heat flux profiles taken from (a) at 2900 ms (solid curve), before the magnetic perturbation pulse and at 3300 ms (dashed curve) during the perturbation pulse.

the error-field correction coil which is typically used on most DIII–D discharges to prevent locked modes due to field-errors) it appears that these heat flux modulations must be due to the slowing down of the internal neoclassical tearing modes (the MHD modes mentioned above) or currents generated in the edge of the plasma such as those measured with the toroidal tile current array.

It should be possible, in future experiments, to simultaneously measure both the edge current and the magnetic field from core MHD modes and to use these fields in TRIP3D_MAP to calculate the structure of the tangles during the slow evolution phase when modulations are observed on the heat flux profiles. Fast imaging cameras, such as the one used on the NSTX machine (a spherical tokamak) [16], looking at divertor deuterium ionization (D_α) emissions also provides important information on the edge magnetic topology of the plasma during ELMs and MHD events and we anticipate the addition of a similar diagnostic for these studies in the near future. Measurements of D_α emissions in the lower divertor of DIII–D with a slow CID camera have resulted in a series of interesting images during the ELM suppression experiments discussed above. As can be seen in Fig. 11, these images also show a characteristic splitting that is well correlated with the magnetic perturbation pulse from the I–coil. The qualitative features of these split divertor target emissions are in agreement with the calculated structure of the homoclinic lobes shown in Fig. 5 but the amplitude of the lobe found using only the perturbation from the I–coil pulse is too small to explain the degree of splitting observed. This suggests that either another perturbation source is contributing to the splitting or the plasma amplifies the applied perturbation by driving currents in the scrape-off layer. The total perturbation field from the I–coil with a current of 4.4 kA is approximately the same size as that due to the measured field-errors in DIII–D so it is conceivable that the splitting from tangles due to field-errors

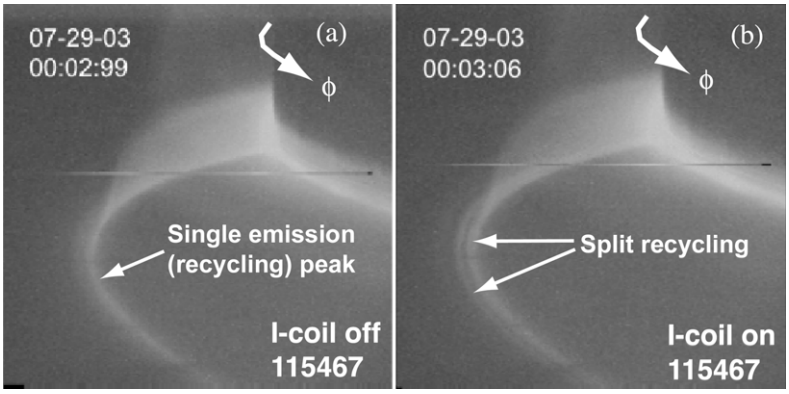

Fig. 11. (a) Visible camera view of the lower divertor in DIII–D using a D_α filter. This image was taken prior (t = 2990 ms) to the I–coil pulse in discharge 115467 and show a single emission line along the divertor target at the location of the outer strike point and (b) the same view as in (a) but taken 60 ms later during the I–coil pulse show a splitting of the emission along the outer strike point tat agrees with the heat flux splitting shown in figure 10.

alone are not resolvable by the camera prior to the I–coil pulse. On the other hand, when the I–coil is applied the magnitude of the perturbation approximately doubles. Calculations of perturbations such as this in TRIP3D_MAP indicate that these could be large enough to produce the splitting observed in the heat flux and divertor emissions but additional calculations are needed to see if the details of the tangles are consistent with both measurements when the amplitudes and phases of the field-errors are combined with the I–coil perturbation field. In some cases currents in the scrape-off layer produce non-axisymmetric magnetic perturbations that are equivalent to or larger than those from the external correction or control coils. Halo currents driven during the current quench phase of most disruptions are an example of the largest scrape-off layer currents measured with the toroidal tile current array in DIII–D. Individual toroidal filaments can exceed several kilo amperes in some types of halo currents. Currents are also measured during ELMs [12,14] and can often exceed 100 amperes per filament. These currents undergo complex space and time variations as the ELM instability evolves. They typically involve multiple filaments that appear to be rotating or undergoing a rapid change in amplitude. An example of the behavior of these currents is given in Fig. 12(a) where we have overlayed the currents measured by six toroidally distributed elements of the toroidal tile current array on a single plot. Here we see a series of large rapid current spikes associated with the ELMs which lead up to the onset of a locked mode starting at t = 1431 ms. At t = 1440–1455 ms the locked mode slowly rotates and locks solidly for about 15 ms at ϕ = 240 deg as shown in Fig. 12(b). This slowly rotating phase of the lock mode is referred to as the quasi-stationary phase of the mode (i.e., a QSM). The toroidal phase angle of the locked mode and QSM is shown in Fig. 12(b) and its amplitude in Fig. 12(c) where we note that the integration time constant of this detector is too slow to see the fast ELM perturbations earlier in the discharge.

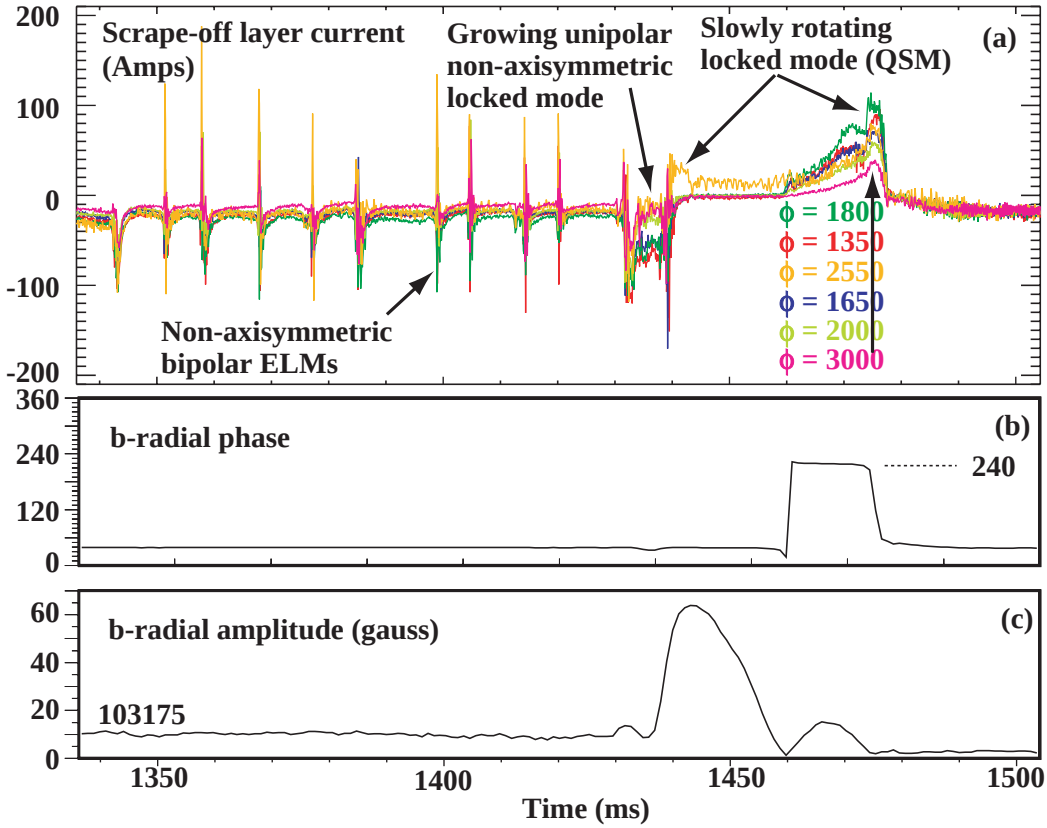

Fig. 12. (a) Slow toroidal tile current array signals from six sensors near the outer strike point in DIII–D discharge 103175. The signals from toroidal angles ϕ = 180, 135, 255, 165, 200, and 300 degs are shown in sequence from top to bottom 1475 ms as indicated by the vertical arrow and (b) toroidal phase angle of the locked mode (QSM) from a set of midplane saddle loops with a relatively long integration time constant and (c) the amplitude of the locked mode from the midplane saddle loop.

Slowly rotating QSMs with relatively long lifetimes are often observed in DIII–D and provide an interesting perturbation source for studying homoclinic tangle structure. An example of a slowly rotating QMS is shown in Fig. 13 where the phase and amplitude of the mode is plotted over a period of 1500 ms. We see that the mode rotates quite slowly, becoming almost stationary near ϕ = 240 deg where the largest components of the field-errors are found in DIII–D and then it rotates rapidly around the machine one full toroidal revolution once it slips past ϕ = 240 deg. The amplitude modulation is well correlated with the change in toroidal phase growing slowly as the mode hesitates at ϕ = 240 deg and dropping rapidly as the mode slips past this preferred phase angle. Most of the QSMs observed in DIII–D display a similar behavior. Figure 14 shows the radial position of the locked mode detector used to study these QSMs and the view used by the IR camera located at ϕ = 165 deg. We use this camera to follow the evolution of the heat flux profiles in the lower divertor during the evolution of the QSM shown in Fig. 13. In Fig. 15 we indicate four times between 3200 and 3260 ms during which the IR camera data was collected. The radial profiles of the heat flux calculated with the IR camera data is shown in Fig. 16. We also show the toroidal angle of the outward pointing magnetic field at the horizontal midplane of DIII–D due to the slowly rotating QSM in the upper right-hand corner of

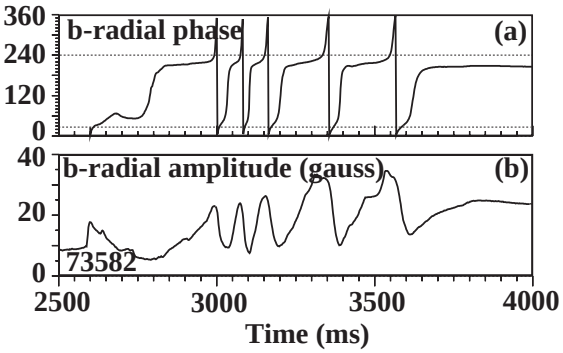

Fig. 13. (a) Toroidal phase angle of a Quasi-Stationary Mode (QSM) in discharge 73582 and (b) the amplitude of the QSM as determined from the locked mode detector shown in Fig. 14.

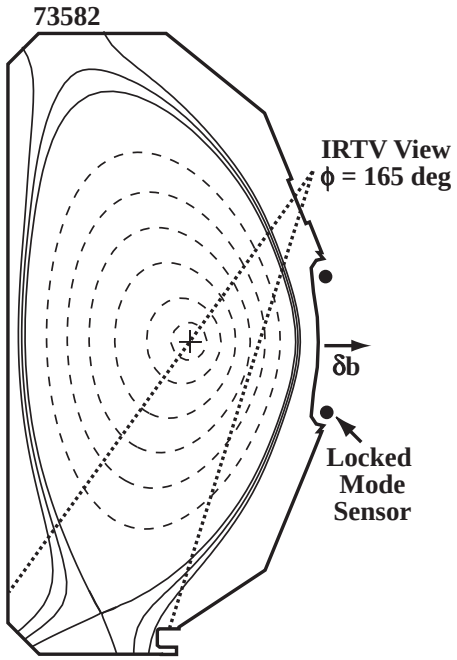

Fig. 14. DIII–D equilibrium shape during the QSM seen in discharge 73582 showing the view used by the infrared TV camera at ϕ = 165 deg and the radial position of the locked mode detector.

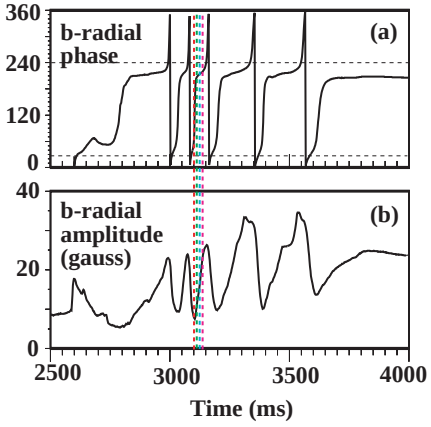

Fig. 15. (a) Toroidal phase angle and (b) amplitude of the Quasi-Stationary Mode (QSM) in discharge 73582 with IR camera data times used in Fig. 16 shown.

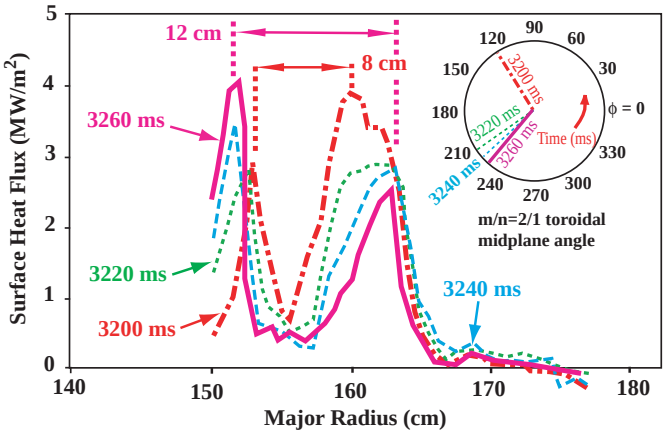

Fig. 16. Changes in the lower divertor heat flux profiles for the times shown in Fig. 15 and the toroidal angle of the QSM is shown in the upper right-hand corner of the figure.

Fig. 16. Here, we see that the mode moves from ϕ = 120 deg to ϕ = 210 deg between the first two 20 ms time slices and then dwells near ϕ = 240 deg for the next three time slices. These data show that the peak-to-peak separation of the double peak heat flux structure increases from ~8 to ~12 cm as the QSM perturbation field rotates past the view of the IR camera. This is consistent with a rotation of the spiral footprint due to a homoclinic tangle (such as the one shown in Fig. 6) in the clockwise direction which is the same direction the QSM rotates in this discharge. The measured increase in the separation of the two peaks is also consistent with the $n=1$ spiral structure of the footprint shown in Fig. 6 and with the toroidal mode number of QSMs in DIII–D which are $m=2$ modes that are located on the $q=2$ resonant surface of the plasma. The subsequent evolution of this mode over the next 60 ms is shown in Fig. 17 and then from 3380 to 3440 ms in Fig. 18. We see in Fig. 17 that the double peak structure of the footprint transitions abruptly to a single peak as the QSM rotates between ϕ = 330 deg at 3300 ms and ϕ = 30 deg at 3320 ms. This behavior is qualitatively in very good agreement with the tip of the spiral (as shown in Fig. 5) produced by an $n=1$ tangle rotating past the view of the IR camera during this time interval. As the mode continues to rotate the double peak structure returns but there are some qualitative differences during the second toroidal revolution as seen in Fig. 18. These difference may be due to changes in the amplitude of the mode on the $q=2$ surface or in the distribution of the scrape-off layer currents being driven through the non-resonant tangles extending out into the scrape-off layer. Additional data and modeling with TRIP3D_MAP is needed to better interpret these differences in the footprint structure.

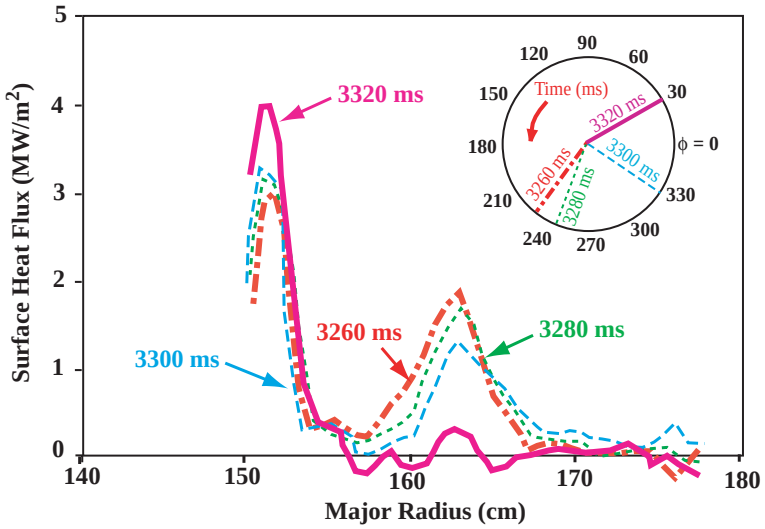

Fig. 17. Changes in the lower divertor heat flux profiles between 3260 and 3320 ms in discharge 73582 and the toroidal angle of the QSM is shown in the upper right-hand corner of the figure.

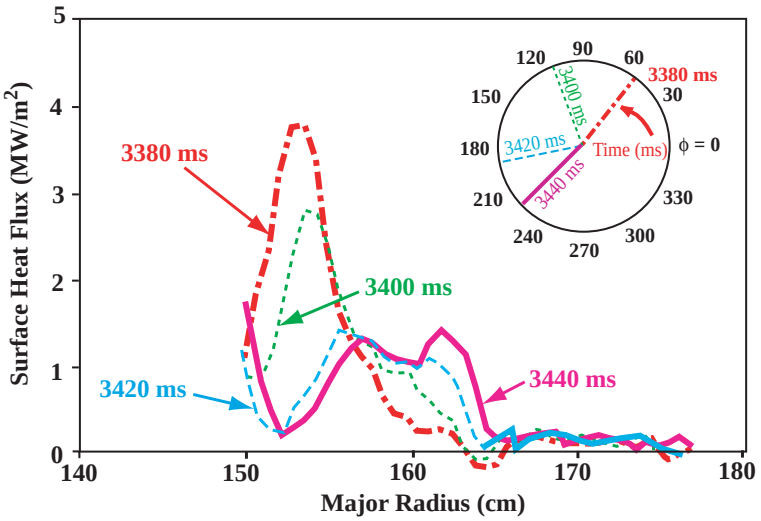

Fig. 18. Changes in the lower divertor heat flux profiles between 3380 and 3440 ms in discharge 73582 and the toroidal angle of the QSM is shown in the upper right-hand corner of the figure.

5. SUMMARY AND CONCLUSIONS

Poloidally diverted plasmas are particularly sensitive to the onset of a class of elementary topological instabilities know as homoclinic tangles that result from the Hamiltonian nature of the vacuum magnetic fields in such systems. These tangles are known to be associated with Hamiltonian chaos in many classical systems [17] and thus are of interest in real physical systems since proof of their existence has important implications for a broad range of physics application. Such instabilities do not require field line tearing and reconnection but simply represent a reconfiguration of the vacuum magnetic topology due to resonant and non-resonant interactions of non-axisymmetric perturbations from either external sources, internal MHD modes or current filaments that form on open field lines connecting to solid surfaces such as divertor target plates or vacuum vessel walls. The topological web of tangles produced by intersections of resonant island tangles with non-resonant separatrix tangles in poloidally diverted tokamaks is typically very complex and quite sensitive to a variety of control parameters such as the shape of the flux surfaces (e.g., triangularity, squareness, relative up-down balance of the equilibrium hyperbolic fixed points etc.). Nevertheless, it has been shown in this paper that a number of experimental measurements made in the DIII–D tokamak agree qualitatively very well with the topology of the tangles calculated with a realistic twist map (TRIP3D_MAP) that accurately models the axisymmetric plasma equilibrium and the full geometry of the external magnetic perturbations due to field-errors, correction coils and control coils.

It is found that non-resonant homoclinic tangles form filament-like structures that protrude out into the scrape-off layer. These filaments, when imaged with cameras looking at deuterium or impurity line emissions, can produce bands of enhanced emission in the divertor region where higher densities of cold neutral atoms are concentrated and will look like fingers reaching radially outward from the region of the unperturbed equilibrium separatrix. Since separatrix tangles are connected to hot plasma in the core, through intersections with resonant island tangles, they will be continuously filled with hot plasma that is transported into the tangle footprints and deposited on solid surfaces such as divertor target plates with a pattern that is characteristic of the tangle topology. Examples of these patterns in DIII–D have been presented in this paper for a case in which the tangles are driven by a current pulse in an externals coil (Figs. 10 and 11) and for a case where an internal mode on the $q = 2$ surface (a Quasi-stationary mode) was present. In both cases the measured pattern is in good qualitative agreement with the calculated structure of the divertor target plate footprint due to the non-resonant tangle. Other examples of heat flux patterns, during ELMs in ASDEX–U [13], with very similar structures to those present here also appear to agree with the basic structure of the tangles although these may require perturbations with higher toroidal mode numbers than those discussed above. Additionally, we note that higher n emission filaments have recently been observed on the MAST tokamak [18] that fit the tangle topology relatively well if one assumes that higher n magnetic perturbations are involved in the ELMs responsible for these emission filaments. Similar measurements have recently been made on NSTX showing a clear $n = 1$ filament protruding into the scrape-off layer during smaller ELM events in this tokamaks [16]. These filaments look very similar to the tangle structures calculated in this paper such as the one shown in Fig. 7.

6. ACKNOWLEDGMENTS

The work discussed in this paper was sponsored by the U. S. Department of Energy under contract Nos. DE-AC03-99ER54463 and W-7405-ENG-48. Support for R. K. W. R. was also provided by a NDSEG Fellowship and for J.A. Carter and B.I. Rapoport through the DOE National Undergraduate Fusion Fellowship Program. We would like to thank R. Moyer and T. Takahashi for helpful discussions of the experimental data presented in this paper.

7. REFERENCES

[1] Guckenheimer J and Holmes P 1983 *Nonlinear Oscillations, Dynamical Systems, and Bifurcations of Vector Fields* Applied Mathematical Science **42** (New York: Springer-Verlag) p 222

[2] Meiss J D 1992 *Rev. Mod. Phys.* **64** 795

[3] Pomphery N and Reiman A 1992 *Phys. Fluids* B **4** 938

[4] Abdullaev S S and Finken K H 1998 *Nucl. Fusion* **38** 531

[5] Evans T E, Moyer R A and Monat P 2002 *Phys. Plasmas* **9** 4957

[6] Lao L, St Johns H, Stambaugh R D, Kellman A G and Pfeiffer W 1985 *Nucl. Fusion* **25** 1611

[7] Luxon J L 2002 *Nucl. Fusion* **42** 614

[8] Evans T E, Roeder R K W, Carter J A and Rapoport B I 2004 *Contrib. Plasmas Phys.* **44** 235

[9] Evans T E 1991 *Proc. 18th EPS Conf. on Controlled Fusion and Plasma Physics (Berlin)* part II p 65

[10] Roeder R K W, Rapoport B I and Evans T E 2003 *Phys. Plasmas* **10** 3796

[11] da Silva E C, Caldas I L, Viana R L and Sanjuán M A F 2002 *Phys. Plasmas* **9** 4917

[12] Evans T E, Lasnier C J, Hill D N, Leonard A W, Fenstermacher M E, Petrie T W and Schaffer M J 1995 *J. Nucl. Mater.* **220-220** 235.

[13] Eich T, Herrmann A, Neuhauser J and ASDEX Upgrade Team 2003 *Phys. Rev. Lett.* **91** 195003-1

[14] Takahashi T, Fredrickson E D, Schaffer M J, Austin M E, Evans T E, Lao L L and Watkins J G 2004 *Nucl. Fusion* **44** 1075

[15] Evans T E, Moyer *et al*., 2004 *Phys. Rev. Lett*. **92** 235003-1

[16] Maingi R, *et al*. "H–mode turbulence, power threshold, ELM, and pedestal studies in NSTX" *Nucl. Fusion* (submitted)

[17] Zaslavsky G M 1998 Physics of Chaos in Hamiltonian Systems (London, U K, Imperial College Press World Scientific Publishing)

[18] Kirk A, Wilson H R, Counsell G F, Akers R, Arends E, Cowley S C, Dowling J, Lloyd B, Price M, Walsh M and MAST Team 2004 *Phys. Rev. Lett*. **92** 245002-1